This Supplementary Information contains Supplementary Notes 1–4 and Supplementary Figures 1–4.

Contents

Supplementary Note 1: Experimental setup and synchronization

Optical trapping. Optical confinement was realized using a 532 nm diode-pumped solid-state laser (Coherent® Verdi-V2). The laser intensity was modulated by an acousto-optic modulator (AA Opto-Electronic® MT80-A1.5-VIS) and directed into the back focal plane of a 100× oil-immersion objective (Zeiss® EC Plan-Neofluar M27, NA = 1.3), creating a harmonic trapping potential. For double-well experiments, the laser focus was oscillated at 700 Hz using a galvanometric mirror to generate a time-shared potential (Supplementary Fig. 1a). This modulation frequency significantly exceeds the particle's corner frequency, ensuring that the tracer experiences a stable, time-averaged conservative potential rather than a dynamically flickering trap.

Imaging and tracking. Particle positions were measured using bright-field imaging with a 470 nm LED illumination source and a 20× condenser objective (Nikon® EPI Plan SLWD, NA = 0.35). Scattered light was collected by the trapping objective and imaged onto a CCD camera (Basler® a2A2600-64umBAS), operated at 100 frames per second with a 150 × 150 pixel region of interest. Tracer particles appeared as bright Gaussian-like spots on a dark background (Supplementary Fig. 1b). Their positions were extracted using a custom tracking algorithm adapted from Ref. [1]. Briefly, raw images were smoothed with a Gaussian kernel, the brightest pixel was identified, and the local intensity distribution was fitted with a second-order polynomial. This procedure yielded a sub-pixel localization accuracy of approximately 6 nm.

Potential reconstruction. The trap stiffness κ and potential geometry were reconstructed from equilibrium position fluctuations via Boltzmann inversion, $V(x) = -k_{\mathrm{B}}T \ln P(x)$, yielding a harmonic potential $V(x) = \frac{1}{2}\kappa x^2$ (Supplementary Figs. 1c,d). The maximum laser power at the sample corresponded to a trap stiffness of approximately 40 µN/m.

Stage and temperature control. The sample chamber was mounted on a piezoelectric translation stage (Piezoconcept® LT3.300), allowing precise and reproducible relative motion between the optical trap and the viscoelastic medium. Temperature stabilization was achieved using an objective heater (Okolab®), which maintained the oil-immersion objective at 25°C. Because the objective is in direct thermal contact with the capillary, the sample region remained thermally stable throughout the experiments.

Hardware synchronization. Real-time feedback protocols required precise temporal synchronization between imaging, laser modulation, and mechanical actuation. This was achieved using two dual-channel function generators (Tektronix® AFG31000), which served as a shared master clock for the experiment. One generator controlled the acousto-optic modulator and piezoelectric stage motion, while the second provided hardware trigger signals for camera acquisition, ensuring deterministic timing and eliminating software-induced jitter between measurement and actuation. To validate synchronization and ensure data integrity, a data acquisition card (National Instruments® USB-6003) continuously recorded the camera exposure signal and the piezo-stage position monitor at a sampling rate of 3 kHz, well above the imaging rate. This high-bandwidth hardware logging enabled each video frame to be unambiguously mapped to the instantaneous trap position, providing a robust temporal reference for state classification, feedback execution, and work calculation.

Supplementary Note 2: Viscoelastic micellar solutions and timescales

Solution preparation. Viscoelastic micellar solutions were prepared by dissolving cetylpyridinium chloride monohydrate (CPyCl, Sigma®, 99%) and sodium salicylate (NaSal, Sigma®, 99.5%) in equimolar proportions in deionized water. Two surfactant concentrations were used in this study: 8 mM for single-well experiments and 5 mM for double-well experiments. For a total solvent mass of 104.4 g, the 8 mM solution was prepared using 286.4 mg of CPyCl and 128.1 mg of NaSal, whereas the 5 mM solution contained 179.0 mg of CPyCl and 80.1 mg of NaSal.

All mixtures were stirred continuously at 100 rpm for 24 h at 45 °C to ensure complete dissolution and homogenization. After preparation, the solutions were cooled to 25 °C and maintained under gentle stirring until use. Under these conditions, the surfactants self-assemble into worm-like micelles forming an entangled network, giving rise to pronounced viscoelastic behavior.

Sample preparation. Silica microspheres of diameter 2.73 µm (microParticles GmbH®) were used as tracer particles and dispersed at low volume fraction to avoid interparticle interactions. For optical trapping experiments, approximately 1 µL of a concentrated microsphere suspension was added to 1 mL of the micellar solution. The suspension was loaded into rectangular borosilicate glass capillaries (VitroTubes®, thickness 100 µm) by capillary action. The open ends were sealed with bee wax (Hampton Research®) and reinforced with a two-component epoxy resin to ensure mechanical stability and chemical inertness. Samples were equilibrated for at least 24 h on a temperature-controlled stage maintained at 25 °C prior to measurements.

Recoil-based characterization. To obtain an estimate of the characteristic viscoelastic relaxation timescales relevant to our experiments, we performed recoil measurements following established protocols reported in our previous works [2, 3]. In these experiments, a trapped particle is translated at a constant velocity v for a duration t using an optical trap, which is then abruptly switched off. For the 5 mM micellar solution, the particle was driven at $v = 3\,\mu\text{m/s}$ for $t = 9\,\text{s}$, whereas for the 8 mM solution is driven at $v = 0.3\,\mu\text{m/s}$ for $t = 60\,\text{s}$. These parameters were chosen to ensure comparable strain amplitudes while remaining within the linear response regime of the viscoelastic bath.

Upon release, the particle exhibits a recoil toward its initial position due to the relaxation of elastic stresses stored in the micellar network. The recoil trajectories display a clear bi-exponential relaxation, reflecting the coexistence of short- and long-time stress relaxation of the micellar network. The extracted fit parameters for both concentrations are summarized in Supplementary Table 1. In the context of the present study, the longer relaxation time provides a relevant estimate of the memory timescale of the bath.

For the 8 mM solution, the long relaxation time is approximately 6 s, while for the 5 mM solution it is shorter, approximately 2.8 s. Mean recoil trajectories for both concentrations are shown in Supplementary Fig. 2, where the black lines indicate ensemble-averaged displacements and the shaded regions denote the standard deviation across 18 and 37 realizations corresponding to 8 mM and 5 mM solutions respectively.

Supplementary Note 3: Statistical uncertainty and control-ensemble construction

Bootstrap resampling. Statistical uncertainties for all experimental observables were quantified using a bootstrap resampling procedure to estimate the error in the mean [4, 5]. For the state-conditioned relaxation curves, which were subsampled from long continuous trajectories, we generated 500 bootstrap realizations by randomly selecting 10^3 segments with replacement. For the work extraction data, where each curve corresponds to a specific measurement delay δt, bootstrapping was performed by generating 2000 resampled datasets. Each dataset was constructed by selecting the maximum number of independent trajectories with replacement from the original ensemble. In both cases, the shaded bands represent the standard deviation of the bootstrap distribution, providing a robust estimate of the standard error of the mean.

Construction of control ensembles. We implement a resampling technique to isolate the contribution of hidden degrees of freedom (hDoF) by constructing a control distribution $\tilde{\rho}_{|ij\rangle}(x,0)$ that matches $\rho_{|ij\rangle}(x,0)$ at $t=0$ but is history-blind. The single-measurement ensemble $|j\rangle$ is partitioned into spatial bins; within each bin b, we denote by n_b the available trajectories and by m_b the subset satisfying the two-measurement condition $|ij\rangle$. The control ensemble is generated by randomly subsampling exactly m_b trajectories from the n_b candidates in each bin. This ensures that at $t=0$, the empirical distribution of particle positions Supplementary Fig. 3 and the initial information $I(0)$ is identical to that of the two-measurement state, $\tilde{\rho}_{|ij\rangle}(x,0)=\rho_{|ij\rangle}(x,0)$, while removing history-dependent selection.

Supplementary Note 4: Markovian Baseline and Numerical Simulations

To confirm that the observed information backflow is a signature of non-Markovian dynamics, we compare our experimental results with a memory-less baseline. In a Markovian system, the particle's evolution is governed solely by the instantaneous potential and thermal fluctuations, with no dependence on the history of the hidden degrees of freedom (hDoF).

Langevin Dynamics Simulation. We modeled the Markovian limit using a standard over-damped Langevin equation:

$$\gamma \dot{x} = -\nabla V(x) + \sqrt{2 k_{\mathrm{B}} T \gamma} \xi(t), \tag{1}$$

where γ is the friction coefficient, $V(x)$ is the harmonic potential, and $\xi(t)$ is Gaussian white noise. The parameters were matched to the experimental single-well trap stiffness (κ), temperature (T) and γ [6] given in Supplementary Table. 2. We applied the identical double-measurement protocol used in the experiments to the simulated trajectories. As shown in Supplementary Fig. 4a, the state-averaged information $I(t)$ (solid line) and the history-blind control $\tilde{I}(t)$ (open circles) are indistinguishable in the simulation. This collapse confirms that for a Markovian system, once the initial position distribution is matched ($\tilde{\rho}_{|ij\rangle}(x, 0) = \rho_{|ij\rangle}(x, 0)$), the future information decay is identical regardless of the system's history.

Validation of Non-Markovianity. To rigorously confirm that the observed information backflow arises from non-Markovian dynamics, we compare the experimental results with a memoryless baseline. In a Markovian system, the future evolution of the particle is determined solely by its instantaneous state, implying that each state-conditioned component $M_{|ij\rangle}$ should vanish. To provide a stringent test, we compute the sum of the absolute values of the components, $\sum_{ij} |M_{|ij\rangle}|$, for the Markovian case. This ensures that each component of the order parameter tends to zero.

As illustrated in Supplementary Fig. 4b, the simulated Markovian sum remains near zero across all delay times δt. In contrast, the experimental data for the 8 mM micellar solution exhibits a pronounced peak in the state-averaged $M(\delta t)$ at $\delta t \approx 1\,\mathrm{s}$. This maximum aligns with the characteristic relaxation timescale of the micellar network, where information stored in the hidden degrees of freedom (hDoF) most strongly influences the particle's subsequent trajectory. The clear divergence between the simulated Langevin dynamics and the experimental observations provides unambiguous evidence for non-Markovian information backflow.

Supplementary Figures

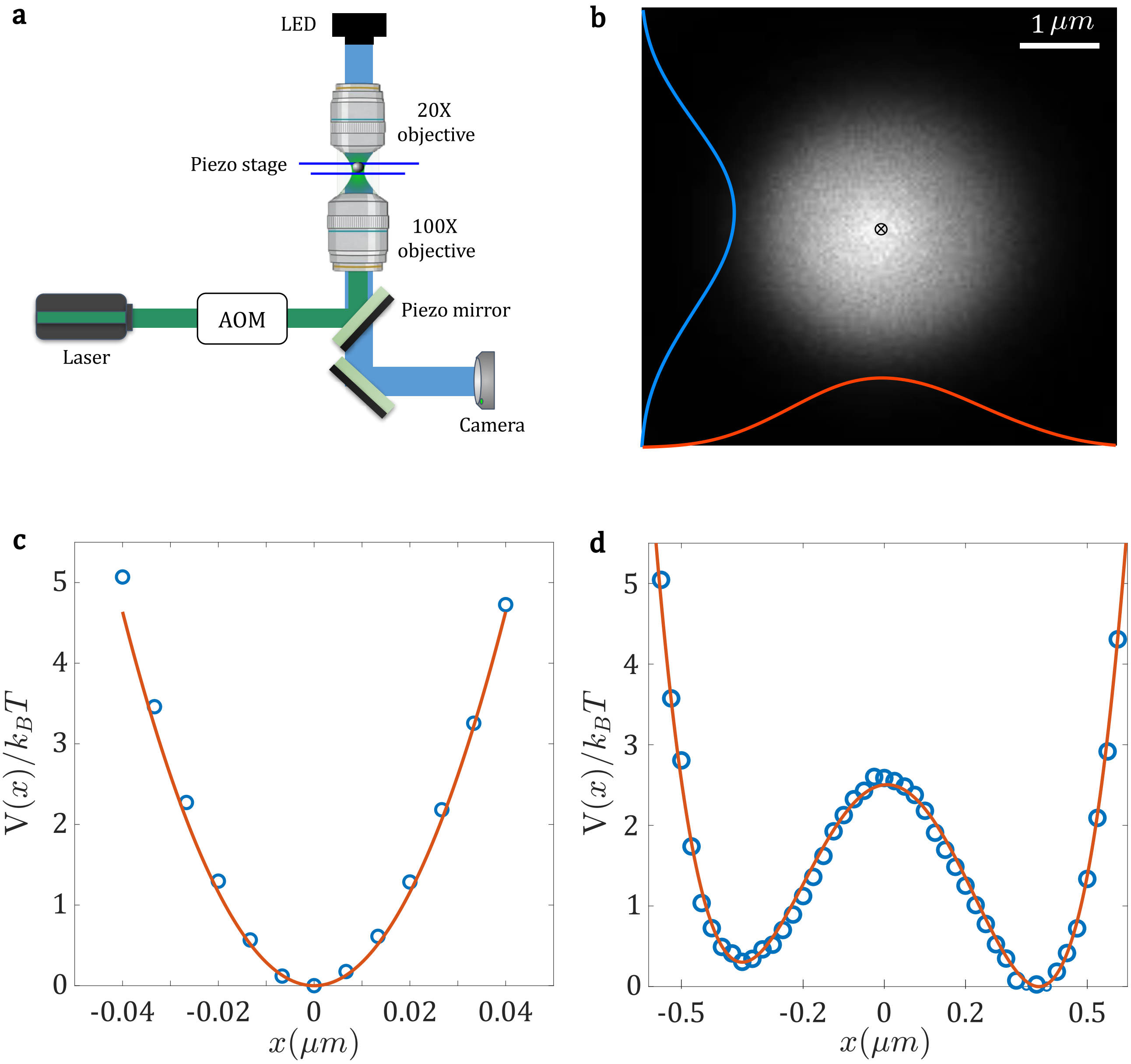

Supplementary Fig. 1 Real-time tracking and potential reconstruction. **a**, Schematic of the experimental setup showing the optical path and imaging system. **b**, CCD image of a single trapped particle with its Gaussian intensity profile, peaking at the particle center. **c**, Reconstructed single-well optical trapping potential and **d**, reconstructed double-well potential obtained from equilibrium position fluctuations.

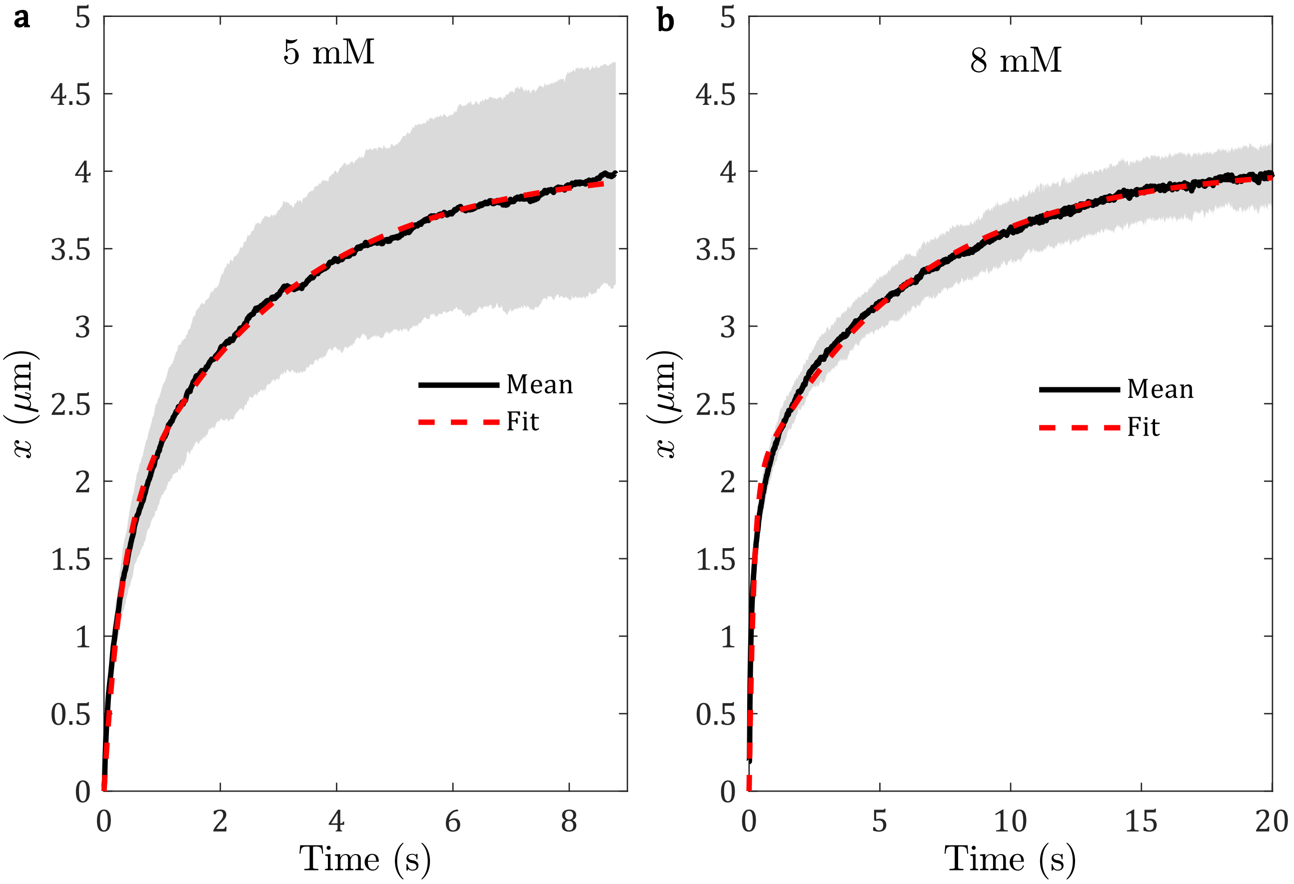

Supplementary Fig. 2 Recoil experiments probing viscoelastic relaxation timescales. **a**, Mean recoil trajectory of an optically trapped particle in the 5 mM micellar solution following sudden trap release after steady translation at constant velocity. The particle was driven at $v = 3\ \mu\mathrm{m\,s}^{-1}$ for 9 s. **b**, Same experiment performed in the 8 mM micellar solution, with driving parameters $v = 0.3\ \mu\mathrm{m\,s}^{-1}$ and 60 s duration. Black solid lines show the mean particle displacement along the driving direction, averaged over repeated realizations, and shaded regions indicate the standard deviation. The recoil dynamics exhibit clear bi-exponential relaxation, with long relaxation times of approximately 2.8 s for 5 mM and 6 s for 8 mM.

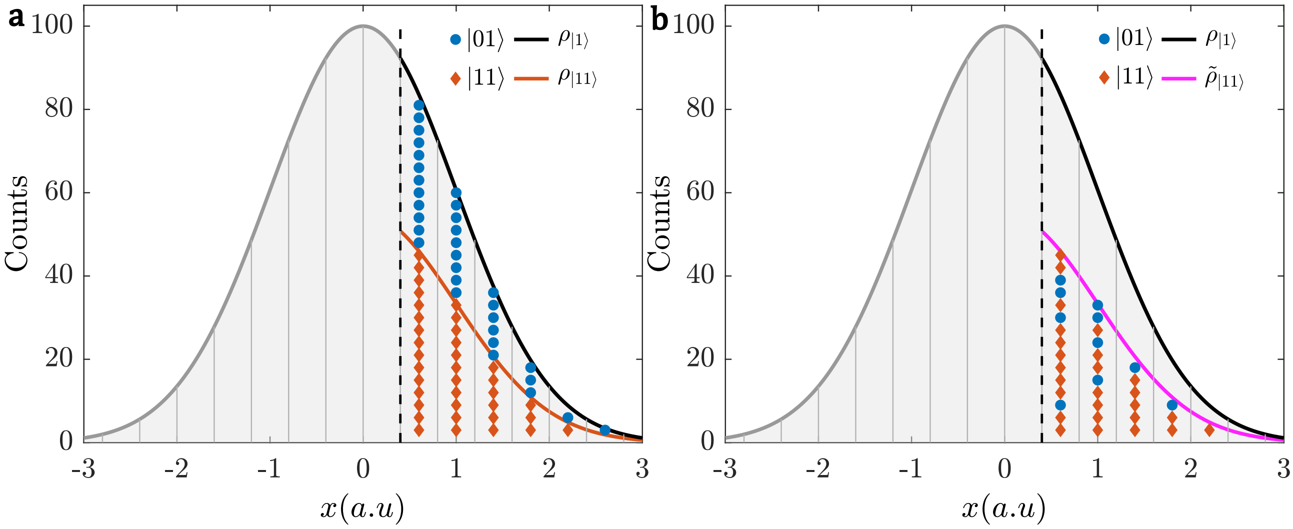

Supplementary Fig. 3 Construction of history-blind control ensembles. **a,** Distribution of the single-measurement state $\rho_{|1\rangle}$ (black curve) and the history-conditioned subset $\rho_{|11\rangle}$ (orange curve). Within each spatial bin to the right of the threshold, the total vertical stack represents n_b trajectories. The orange diamonds denote the specific subset m_b that satisfied the $|11\rangle$ condition at the previous measurement time, while blue circles represent the remainder of the $|1\rangle$ ensemble, $|01\rangle$. **b,** Construction of the control ensemble $\tilde{\rho}_{|11\rangle}$. The distribution is formed by randomly subsampling m_b trajectories from the total available pool in each bin. This results in a mixed composition of circles and diamonds, ensuring the ensemble is history-blind while maintaining a spatial density and initial information $I(0)$ identical to the original two-measurement state.

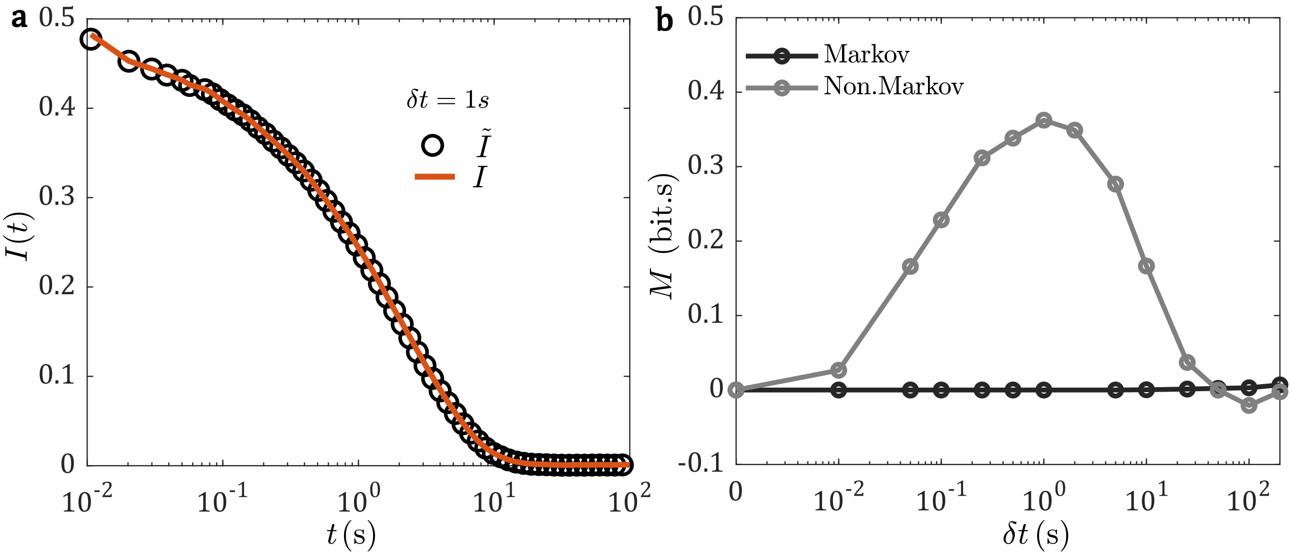

Supplementary Fig. 4 Validation of non-Markovianity against Langevin simulations. a, State-averaged information decay $I(t)$ for the Markovian case. The solid line represents the double-measurement information $I(t)$, while open circles represent the history-blind control $\tilde{I}(t)$ derived from simulated Langevin trajectories. The perfect overlap confirms that history does not influence information decay in memory-less systems. **b,** Integrated order parameter $M(\delta t)$ as a function of measurement delay. The black markers (Markov Sim.) represent the sum of the absolute values of state-conditioned components $\sum |M_{|ij\rangle}|$, which remains zero across all δt. The gray markers (Non-Markov Exp.) show the state-averaged experimental data $M(\delta t)$ for the8 mM solution. The pronounced maximum at $\delta t \approx 1\,\mathrm{s}$ identifies the temporal window where the hidden degrees of freedom of the micellar network exert the strongest influence on the particle's relaxation.

Supplementary Tables

Supplementary Table 1 Double-exponential fit parameters for the recoil curves at 5 mM and 8 mM. The fit function is $x(t) = a - a_1 e^{-t/\tau_1} - (a - a_1)e^{-t/\tau_2}$.

Conc. (mM)	a (µm)	a_1 (µm)	τ_1 (s)	τ_2 (s)
5	4.04	1.60	0.285	2.89
8	4.03	1.98	0.173	6.04

Supplementary Table 2 Simulation parameters for markovian system

Parameter	Symbol	Value
Trap stiffness	κ	1.9×10^{-6} N/m
Temperature	T	298 K
Drag coefficient	γ	6.3×10^{-6} kg/s

References

[1] J. C. Crocker and D. G. Grier, Journal of colloid and interface science **179**, 298 (1996).

[2] F. Ginot, J. Caspers, L. F. Reinalter, K. K. Kumar, M. Krüger, and C. Bechinger, New Journal of Physics **24**, 123013 (2022).

[3] J. Caspers, N. Ditz, K. Krishna Kumar, F. Ginot, C. Bechinger, M. Fuchs, and M. Krüger, The Journal of Chemical Physics **158** (2023).

[4] A. C. Davison and D. V. Hinkley, *Bootstrap methods and their application*, 1 (Cambridge university press, 1997).

[5] T. J. DiCiccio and B. Efron, Statistical science **11**, 189 (1996).

[6] F. Ginot and C. Bechinger, Nature Communications **16**, 10114 (2025).